



Liquid exfoliation of $g\text{-C}_3\text{N}_4$ nanosheets to construct 2D-2D $\text{MoS}_2/g\text{-C}_3\text{N}_4$ photocatalyst for enhanced photocatalytic H_2 production activity

Yong-Jun Yuan^{a,*}, Zikhai Shen^a, Shiting Wu^a, Yibing Su^b, Lang Pei^a, Zhenguo Ji^{a,*}, Mingye Ding^a, Wangfeng Bai^a, Yifan Chen^{a,c}, Zhen-Tao Yu^{b,*}, Zhigang Zou^{b,d}

^a College of Materials and Environmental Engineering, Hangzhou Dianzi University, Hangzhou 310018, People's Republic of China

^b National Laboratory of Solid State Microstructures and Collaborative Innovation Center of Advanced Microstructures, Jiangsu Key Laboratory for Nano Technology, College of Engineering and Applied Science, Nanjing University, Nanjing 210093, People's Republic of China

^c State Key Laboratory of Silicon Materials, School of Materials Science & Engineering, Cyrus Tang Center for Sensor Materials and Applications, Zhejiang University, Hangzhou, Zhejiang 310027, People's Republic of China

^d Macau Institute of Systems Engineering, Macau University of Science and Technology, Macau 999078, People's Republic of China



ARTICLE INFO

Keywords:

Photocatalysis
Hydrogen generation
2D photocatalyst
Graphitic carbon nitride
Molybdenum disulfide

ABSTRACT

Although graphitic carbon nitride ($g\text{-C}_3\text{N}_4$) is an attractive photocatalyst for solar H_2 generation, the preparation of $g\text{-C}_3\text{N}_4$ nanosheets via a "green" and simple method as well as the construction of highly-efficient $g\text{-C}_3\text{N}_4$ -based photocatalysts are still challenges. In this study, $g\text{-C}_3\text{N}_4$ nanosheets prepared by a simple probe sonication assisted liquid exfoliation method were used to construct 2D-2D $\text{MoS}_2/g\text{-C}_3\text{N}_4$ photocatalyst for photocatalytic H_2 production. The 2D-2D $\text{MoS}_2/g\text{-C}_3\text{N}_4$ photocatalyst containing 0.75% MoS_2 showed the highest H_2 evolution rate of $1155 \mu\text{mol}\cdot\text{h}^{-1}\cdot\text{g}^{-1}$ with an apparent quantum yield of 6.8% at 420 nm monochromatic light, which is much higher than that of the optimized 0D-2D $\text{Pt}/g\text{-C}_3\text{N}_4$ photocatalyst. The high photocatalytic H_2 production activity of 2D-2D $\text{MoS}_2/g\text{-C}_3\text{N}_4$ photocatalyst can be attributed to the large surface area and the formed 2D interfaces between MoS_2 and $g\text{-C}_3\text{N}_4$ nanosheets. As demonstrated by photoluminescence quenching and time-resolved fluorescence decay studies, the 2D interfaces can accelerate the photoinduced charge transfer, resulting in the high photocatalytic H_2 production performance. This study provides a new strategy in developing highly-efficient $g\text{-C}_3\text{N}_4$ -based photocatalysts for H_2 production via using 2D nanojunction as a bridge to promote the photoinduced charge separation and transfer.

1. Introduction

Solar H_2 generation via artificial photosynthesis is currently an attractive research area owing to its potential to obtain carbon-free hydrogen fuel [1–3]. The challenge for the practical application of photocatalysis is to explore efficient photocatalysts with suitable bandgap, low-cost and excellent durability. Among various semiconductors developed, visible-light-responsive graphitic carbon nitride ($g\text{-C}_3\text{N}_4$) with suitable band edge position has been reported as an active photocatalyst [4–6]. The bulk $g\text{-C}_3\text{N}_4$ photocatalyst prepared via conventional solid-phase polycondensation of organic precursors containing both carbon and nitrogen exhibits relatively large size and small surface area because the resulted polymer tends to agglomerate at high temperature, resulting in the poor photocatalytic performance of bulk $g\text{-C}_3\text{N}_4$. Regulating the morphology of $g\text{-C}_3\text{N}_4$ to quasi-2D nanosheets is an efficient strategy to prepare well-defined $g\text{-C}_3\text{N}_4$ nanostructures with

large surface area and abundant active sites [7–10]. As compared to bulk $g\text{-C}_3\text{N}_4$, the 2D $g\text{-C}_3\text{N}_4$ nanosheets exhibit some apparent advantages including much larger specific surface area and shorter bulk diffusion length, which can provide more abundant reactive sites for H_2 generation reaction and reduce the recombination probability of photogenerated charge carriers, respectively.

Recently, many strategies have been used to synthesize $g\text{-C}_3\text{N}_4$ nanosheets [11–13]. For example, single atomic layered $g\text{-C}_3\text{N}_4$ nanosheets can be prepared by a chemical exfoliation method in presence of concentrated sulphuric acid as the solvent [14,15]. During this process, the NH/NH_2 hydrogen bonds between strands of polymeric melon units were destroyed by the strong acid, breaking the planar cohesion of $g\text{-C}_3\text{N}_4$. Furthermore, Liu et al found the fabrication of $g\text{-C}_3\text{N}_4$ nanosheets via an easy thermal exfoliation method from bulk $g\text{-C}_3\text{N}_4$ [16]. Obviously, those mentioned-above preparation methods suffer from extremely harsh conditions. To develop new simple and

* Corresponding authors.

E-mail addresses: yjyuan@hdu.edu.cn (Y.-J. Yuan), jizg@hdu.edu.cn (Z. Ji), yuzt@nju.edu.cn (Z.-T. Yu).

green strategy with the aim to prepare well-defined $g\text{-C}_3\text{N}_4$ nanostructures with large surface area and abundant active sites, Yang et al., have reported the successful preparation of $g\text{-C}_3\text{N}_4$ nanosheets from bulk $g\text{-C}_3\text{N}_4$ via a simple and cost-effective liquid exfoliation method, and the $g\text{-C}_3\text{N}_4$ nanosheets can act as an efficient photocatalyst for H_2 production due to its unique structure features including the minimal thickness, large aspect ratios and favorable bandgap. More importantly, the $g\text{-C}_3\text{N}_4$ nanosheets can provide ample surface for the growth of cocatalyst to construct 2D-2D photocatalysts. This smart structure with large interfaces can provide abundant channel for charge transfer, which is favorable to enhance the photocatalytic performance of $g\text{-C}_3\text{N}_4$ [17]. Inspired by this conception, we report the design and preparation of 2D-2D $\text{MoS}_2/g\text{-C}_3\text{N}_4$ phootocatalyst for enhanced photocatalytic H_2 production, in which the $g\text{-C}_3\text{N}_4$ nanosheets prepared by a scalable and “green” probe sonication assisted liquid exfoliation method is an excellent support for the growth of MoS_2 cocatalyst. The few-layer MoS_2 was used as a cocatalyst to enhance the photocatalytic activity of $g\text{-C}_3\text{N}_4$ nanosheets owing to its unique properties, such as cost-effective noble-metal-free composition, high reactivity as well as suitable energy band positions [18–21]. As expected, the 2D-2D $\text{MoS}_2/g\text{-C}_3\text{N}_4$ nanosheets showed the highest photocatalytic performance with a H_2 generation rate of $1155 \mu\text{mol h}^{-1} \text{g}^{-1}$, 2.29 times as much as that of MoS_2 loaded bulk $g\text{-C}_3\text{N}_4$. The apparent quantum yield at 420 nm reaches 6.8%. This work can provide new insights into the synthesis of efficient and low-cost semiconductor-based photocatalysts via an eco-friendly method for solar H_2 evolution using 2D nanojunction as a bridge to accelerate the charge transfer in the nanocomposite photocatalysts.

2. Experimental Section

2.1. Materials

All chemical reagents are of analytic grade and were used as received without further purification.

2.2. Synthesis of $g\text{-C}_3\text{N}_4$ nanosheets

Bulk $g\text{-C}_3\text{N}_4$ was prepared by direct heating of urea. In a typical process, 10 g of urea was placed in a crucible with a cover, which was annealed at 550 °C for 3 h. Then, the bulk $g\text{-C}_3\text{N}_4$ powder dispersed in *N*-Methyl pyrrolidone (NMP) solution was ultrasonically treated in a 150 W JY96-IIIN ultrasonic cell disruptor (Fuxi, Shanghai) for 10 h at a temperature below 5 °C in an ice bath. The pulsed ultrasonic irradiation was operated for 4 s on and 2 s off. The larger $g\text{-C}_3\text{N}_4$ particles were removed by centrifugation of the suspension at 4000 rpm for 10 min, the resulted suspension solution was centrifuged at 10,000 rpm for 10 min to obtain the $g\text{-C}_3\text{N}_4$ nanosheets.

2.3. Synthesis of $\text{MoS}_2/g\text{-C}_3\text{N}_4$ nanosheets photocatalysts

The $\text{MoS}_2/g\text{-C}_3\text{N}_4$ nanosheets composites were prepared via a solvent-thermal method. Briefly, 100 mg $g\text{-C}_3\text{N}_4$ nanosheets was added to DMF solution containing a certain concentration of ammonium tetrathiomolybdate $[(\text{NH}_4)_2\text{MoS}_4]$ forming suspension solution. Afterward, the mixed solution was transferred into a Teflon-lined stainless steel autoclave, which was then sealed at 210 °C for 24 h. After the autoclave was cooled to room temperature naturally, the gray product was obtained by centrifugation of the suspension at 10,000 rpm for 10 min, and then dried in a vacuum oven at 60 °C after washed with ethanol for three times.

2.4. Photocatalytic hydrogen production

Photocatalytic H_2 production experiments were carried in a 350 ml outer-irradiation Pyrex photoreactor connected to a glass closed

circulation system. Typically, 50 mg of photocatalyst was dispersed in 250 ml 0.1 M TEOA aqueous solution, the mixed solution was thoroughly degassed several times to remove the dissolved air completely. Then photoreactor was irradiated by a 300 W Xenon lamp equipped with a UV cutoff filter ($\lambda > 420 \text{ nm}$), the amount of evolved H_2 was determined by an on-line gas chromatography (CG1690, Jiedao, TCD, 5 Å molecular sieves column) using argon as the carrier gas. During the photocatalytic reaction, the temperature of solution was kept below 293 K by a cooling water bath. The apparent quantum yield (APY) of photocatalytic system at 420 nm was performed under the same photoreaction condition expect the Xe lamp equipped with a monochromatic light filter ($\lambda = 420 \pm 5 \text{ nm}$), which was calculated by the following equations:

$$\text{AQY}[\%] = \frac{n_{\text{photons}} = \frac{P\lambda}{hc} \times t}{\text{number of reacted electrons}} \times 100 \quad (1)$$

$$= \frac{2 \times \text{number of evolved H}_2 \text{ molecules}}{\text{number of incident photons}} \times 100 \quad (2)$$

where P , λ , h , c and t are the incident light power, wavelength of incident light (420 nm), Planck's constant, velocity of light and illumination time, respectively. The power incident light was measured by an optical power meter (Newport 843-R).

2.5. Structural characterization

The morphology of all samples was characterized by Carl Zeiss Gemini ultra55 field emission scanning electron microscope (SEM, Germany) and transmission electron microscopy (TEM, JEOL JEM 2010, 200 kV). The SEM and TEM samples were prepared by drop-casting dispersion onto a silicon wafer and carbon grid, respectively. X-ray diffraction patterns were collected on a Rigaku-miniflex6 X-ray diffractometer with $\text{Cu K}\alpha$ radiation ($\lambda = 0.15406 \text{ nm}$, 40 kV, 15 mA), recorded with 2θ ranging from 10 to 80° with a scan rate of $10^\circ \text{ min}^{-1}$ and a step size of 0.2°. The morphology and thickness of $g\text{-C}_3\text{N}_4$ nanosheets were studied on a Bruker Multimode 8 atomic force microscopy. The specific surface area was determined from the N_2 adsorption-desorption isotherms according to the Brunauer-Emmett-Teller (BET) method on a Quantachrome Quadrasorb SI porosimeter. Prior to measurements, all samples were degassed at 200 °C for 3 h under nitrogen atmosphere. Photoluminescence and time-resolved fluorescence decay spectra were performed on (FLS980) photospectrometer (Edinburgh Instruments, Edinburgh, Britain). X-ray photoelectron spectroscopy was performed on a VG ESCALAB MKII X-ray photoelectron spectrometer equipped with a monochromatic $\text{Al K}\alpha$ X-ray source, and all the binding energies were calibrated by using the C 1 s peak at 284.8 eV as the reference. Raman spectra were measured on a Horiba LabRam HR instrument equipped with a 532 nm wavelength laser. The UV-vis diffused reflectance spectra (UV-vis DRS) of all samples were obtained by a Shimadzu UV-2550 spectrophotometer. The linear sweep voltammetry (LSV) curves were investigated on a CHI660E electrochemical workstation (Shanghai Chenhua, China) with a standard three-electrode system in 0.5 M Na_2SO_4 aqueous solution using a Ag/AgCl electrode as the reference electrode, Pt wire as the counter electrode and sample-coated glassy carbon (GC) as the working electrode. To prepare working electrode, 4 mg composite and 10 μL 5 wt% Nafion solution were dispersed in 0.4 ml ethanol by at least 0.5 h sonication to form a homogeneous ink. Then, 10 μL of the resulted ink was loaded onto the glassy carbon, which was dried naturally. The Mott-Schottky plots were recorded on an electrochemical workstation (CHI 660E, CHI Instruments, Shanghai, China) by using the Impedance-Potential technique in a conventional three-electrode cell described above, and the 0.5 M Na_2SO_4 aqueous solution was used as the electrolyte.

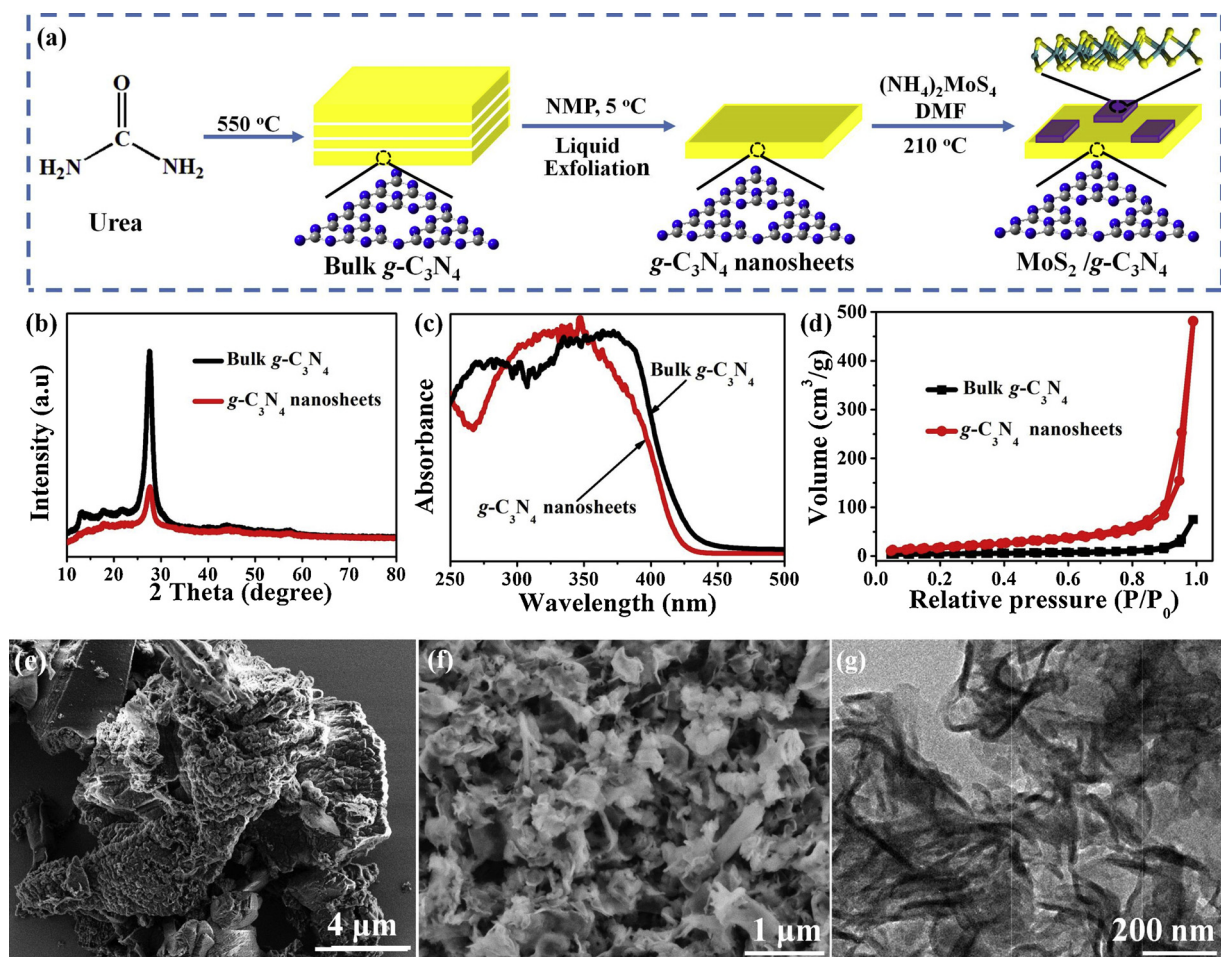


Fig. 1. (a) Schematic diagram of the synthesis of $\text{MoS}_2/\text{g-C}_3\text{N}_4$ nanosheets photocatalysts. (b) XRD patterns of bulk $\text{g-C}_3\text{N}_4$ and $\text{g-C}_3\text{N}_4$ nanosheets. (c) Absorption spectrum of bulk $\text{g-C}_3\text{N}_4$ and $\text{g-C}_3\text{N}_4$ nanosheets. (d) N_2 adsorption-desorption isotherms bulk $\text{g-C}_3\text{N}_4$ and $\text{g-C}_3\text{N}_4$ nanosheets. (e) SEM image of bulk $\text{g-C}_3\text{N}_4$. (f) SEM image of $\text{g-C}_3\text{N}_4$ nanosheets. (g) TEM image of $\text{g-C}_3\text{N}_4$ nanosheets.

3. Results and discussions

As illustrated in Fig. 1a, the $\text{MoS}_2/\text{g-C}_3\text{N}_4$ nanosheets were prepared via a three-step reaction process. Firstly, the yellow bulk $\text{g-C}_3\text{N}_4$ was fabricated by a traditional thermal polymerization method according to a previously-reported study [22]. Then, the $\text{g-C}_3\text{N}_4$ nanosheets were obtained through liquid exfoliation of bulk $\text{g-C}_3\text{N}_4$ in *N*-methyl pyrrolidone (NMP) solution. Finally, solvent-thermal treatment of $\text{g-C}_3\text{N}_4$ nanosheets and $(\text{NH}_4)_2\text{MoS}_4$ in a DMF solvent was used to the form $\text{MoS}_2/\text{g-C}_3\text{N}_4$ composites (denoted as 1.00 wt% $\text{MoS}_2/\text{g-C}_3\text{N}_4$ consisting of 1.00 wt% MoS_2 and 99.00 wt% $\text{g-C}_3\text{N}_4$, for details, see experimental section). The X-Ray diffraction (XRD) patterns of as-prepared $\text{g-C}_3\text{N}_4$ nanosheets as well as bulk $\text{g-C}_3\text{N}_4$ are shown in Fig. 1b. The bulk $\text{g-C}_3\text{N}_4$ shows two distinct peaks at 13.3 and 27.4°, which can be assigned to the (100) and (002) peak of graphitic carbon nitride (JCPDS No.87–1526), respectively [23]. The (002) peak is a characteristic interlayer stacking reflection of conjugated aromatic systems exhibited in bulk $\text{g-C}_3\text{N}_4$ [24]. After exfoliation, the intensity of this (002) peak of the $\text{g-C}_3\text{N}_4$ nanosheets sample significantly decreases, indicating that the nanosheets have been successfully exfoliated from bulk $\text{g-C}_3\text{N}_4$ as expected. This is consistent with the observation from SEM and TEM images, as discussed later. The UV-vis diffuse reflectance spectroscopy illustrated in Fig. 1c shows an obvious blue-shift for $\text{g-C}_3\text{N}_4$ nanosheets sample as compare to that of bulk $\text{g-C}_3\text{N}_4$, and the optical bandgap of $\text{g-C}_3\text{N}_4$ nanosheets and bulk $\text{g-C}_3\text{N}_4$ determined from the $(\alpha h\nu)^{1/2}$ vs. photon energy ($h\nu$) plot was estimated to be approximately to 2.86 and 2.73 eV, respectively (Figure S1). The increased bandgap of $\text{g-C}_3\text{N}_4$

nanosheets can be attributed to the quantum size effect related to its decreasing layers [25]. Furthermore, the N_2 absorption-desorption isotherms show the BET specific surface area of $\text{g-C}_3\text{N}_4$ nanosheets increase to 94.87 m² g⁻¹, which is much higher than that of bulk $\text{g-C}_3\text{N}_4$ sample with a value of 14.81 m² g⁻¹ (Fig. 1d). The morphology feature of $\text{g-C}_3\text{N}_4$ nanosheets was firstly verified by

SEM characterization. Fig. 1e shows the SEM image of the as-prepared bulk $\text{g-C}_3\text{N}_4$, in which the product is layer-like assemblies with a particle size of large than 20 μm. After ultrasonic treatment, the SEM (Fig. 1f) and TEM (Fig. 1g) images shows that the $\text{g-C}_3\text{N}_4$ nanosheets having widths and lengths in the region of 400–800 nm, and the thickness of $\text{g-C}_3\text{N}_4$ nanosheets estimated from the TEM images (Figure S2) of $\text{g-C}_3\text{N}_4$ nanosheets was estimated to be approximately 10 nm. The morphology feature of $\text{g-C}_3\text{N}_4$ nanosheets was then verified by AFM characterization. As illustrated in Fig. 2a, the layered structure can be seen clearly in the AFM image, and the thickness of $\text{g-C}_3\text{N}_4$ nanosheets is around 8–10 nm (Fig. 2b), which is close to that of TEM analysis. The AFM, SEM and TEM results indicate that the $\text{g-C}_3\text{N}_4$ nanosheets have been prepared successfully by liquid exfoliation method. Although the $\text{g-C}_3\text{N}_4$ nanosheets can be exfoliated from bulk $\text{g-C}_3\text{N}_4$, the surface groups have not changed obviously, as confirmed by the FT-IR analysis illustrated in the Figure S3.

After solvent-thermal treatment, the MoS_2 nanosheets were grown on the surface of $\text{g-C}_3\text{N}_4$ nanosheets. Although the MoS_2 was not be observed in the XRD patters (Fig. 3a) of $\text{MoS}_2/\text{g-C}_3\text{N}_4$ composites related to the small amount of MoS_2 , it can be observed by the UV-vis, Raman, EDS, HRTEM and XPS analysis, as discussed later. Fig. 3b shows

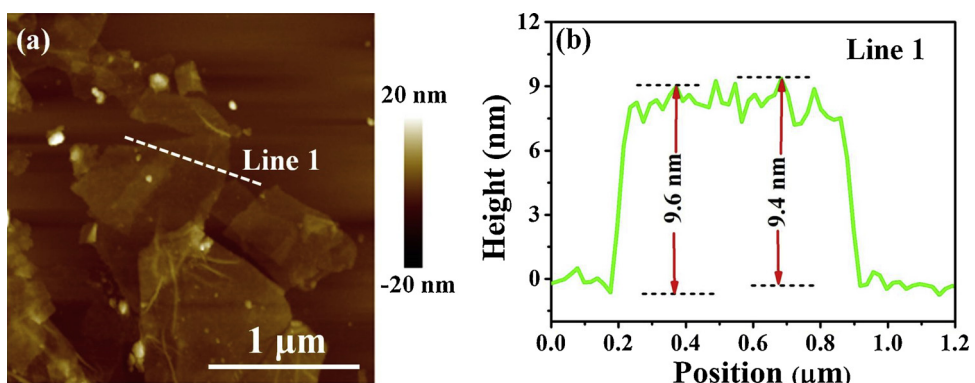


Fig. 2. (a) AFM image of $g\text{-C}_3\text{N}_4$ nanosheets. (b) Height profiles along the white line 1 in Fig. 2(a).

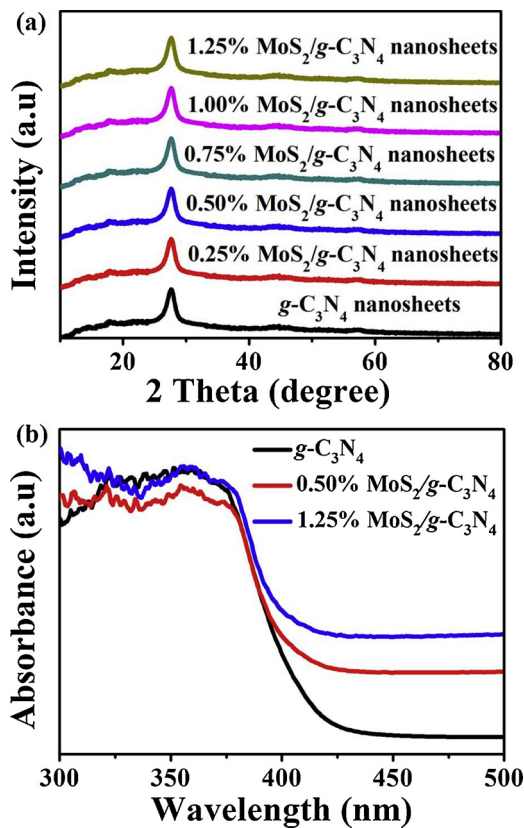


Fig. 3. (a) UV-vis absorption spectra of $g\text{-C}_3\text{N}_4$ and MoS₂/g-C₃N₄ composites. (b) XRD patterns of MoS₂/g-C₃N₄ composites loaded with various amounts of MoS₂.

the absorption spectra of bare $g\text{-C}_3\text{N}_4$ nanosheets, 0.75% and 1.25% MoS₂/g-C₃N₄ nanosheets composites. The bare $g\text{-C}_3\text{N}_4$ nanosheets exhibited absorption only at $\lambda < 450$ nm. In the spectra of MoS₂/g-C₃N₄ nanosheets composites, a significant increase in the visible light region was observed in the UV-vis diffuse reflectance spectra, which is related to the presence of black MoS₂. The Raman analysis of MoS₂/g-C₃N₄ nanosheets (Figure S4) shows two characteristic bands at 377.6 and 401.8 cm^{-1} , corresponding to the in-plane E_{2g} and out-of-plane A_{1g} modes of 2H-MoS₂, respectively, confirming the presence of 2H-MoS₂ in the MoS₂/g-C₃N₄ nanosheets composite [26]. The SEM images of MoS₂/g-C₃N₄ nanosheets illustrated in Fig. 4a and b shows that the composites exhibit similar morphology with that of bare $g\text{-C}_3\text{N}_4$ nanosheets, indicating the structure of $g\text{-C}_3\text{N}_4$ nanosheets remains unchanged after the solvent-thermal treatment. As shown in Fig. 4c, the EDS mapping images of MoS₂/g-C₃N₄ composites demonstrate that the C, N, Mo and S

elements are homogeneously distributed. Furthermore, few-layer MoS₂ can be observed clearly on the surface of $g\text{-C}_3\text{N}_4$ nanosheets in the TEM images of MoS₂/g-C₃N₄ composite (Fig. 4d and e). The HRTEM images of 0.75% MoS₂/g-C₃N₄ composite illustrated

in Fig. 4f shows the lattice fringes of MoS₂ with d spacing of ca. 0.61 nm, which can be attributed to the (001) lattice plane of hexagonal MoS₂ crystal [27]. The XPS survey spectra of 0.75% MoS₂/g-C₃N₄ nanosheets (Figure S5) indicates that C, N, Mo and S elements are observed and their corresponding binding energies are 288.1, 398.9, 229.2 and 162.1 eV, respectively [28,29]. The atomic ratio of Mo to S is ca. 0.48, which is close to in the nominal atomic composition of MoS₂. In the C 1s spectrum (Fig. 5a), two mainly peaks centering at 284.6 eV and 288.0 eV are attributed to the standard carbon (C–C bonds) and the sp²-hybridized carbon (N–C = N). The N 1s peaks (Fig. 5b) can be deconvoluted to two peaks at 399.1 and 401.2 eV, which can be assigned to the C=N=C and N-(C₃) groups, respectively. In the Mo 3d region as illustrated in Fig. 5c, the deconvolution peaks of Mo 3d_{5/2} and 3d_{3/2} were observed at 229.8 and 231.2 eV [30].

The S 2p spectra of MoS₂ consist of peaks at 161.6 and 162.5 eV, which is assigned to the S 2p_{3/2} and S 2p_{1/2}, respectively (Fig. 5d) [31]. All these above characterizations suggest that the MoS₂ has been grown on the surface of $g\text{-C}_3\text{N}_4$ successfully.

As discussed above, the as-prepared MoS₂/g-C₃N₄ nanosheets exhibit 2D superstructure with large surface area, rendering it an excellent candidate for photocatalytic H₂ production. The photocatalytic performance of MoS₂/g-C₃N₄ nanosheets photocatalysts was evaluated and compared to that of bulk material in triethanolamine (TEOA) aqueous solution under visible light irradiation. As illustrated in Fig. 6a, the H₂ evolution rate of the bare bulk $g\text{-C}_3\text{N}_4$ and $g\text{-C}_3\text{N}_4$ nanosheets sample was measured to be 25 and 73 $\mu\text{mol h}^{-1} \text{g}^{-1}$, respectively. After modified

with 0.75% MoS₂, the photocatalytic performance of both bulk $g\text{-C}_3\text{N}_4$ and $g\text{-C}_3\text{N}_4$ nanosheets were remarkably enhanced, and the H₂ generation rate increased to 505 and 1155 $\mu\text{mol h}^{-1} \text{g}^{-1}$, respectively. Although the bulk $g\text{-C}_3\text{N}_4$ has a stronger absorption in visible light region (Fig. 1c), the $g\text{-C}_3\text{N}_4$ nanosheets sample shows a much higher photocatalytic activity for H₂ evolution, which could be attributed to its much larger surface area (Fig. 1d). Furthermore, the $g\text{-C}_3\text{N}_4$ nanosheets is an excellent support for the growth of MoS₂, resulting in the higher H₂ evolution rate of MoS₂/g-C₃N₄ nanosheets. To further confirm the effect of MoS₂ on their photocatalytic activities, we also carried out comparison tests using MoS₂/g-C₃N₄ nanosheets composites with various amounts of MoS₂ as photocatalysts. The bare MoS₂ was demonstrated to be an inactive photocatalyst for H₂ production, which could be related to its poor crystallinity and abundant defect. As shown in Fig. 6b, the bare $g\text{-C}_3\text{N}_4$ nanosheets exhibits low photocatalytic activity. When integrated with cocatalyst, the H₂ evolution rate increase 3.5, 9.4 and 15.8 times for 0.25%, 0.50% and 0.75% MoS₂/g-C₃N₄ nanosheets photocatalysts, respectively. The 0.75% MoS₂/g-C₃N₄ nanosheets shows

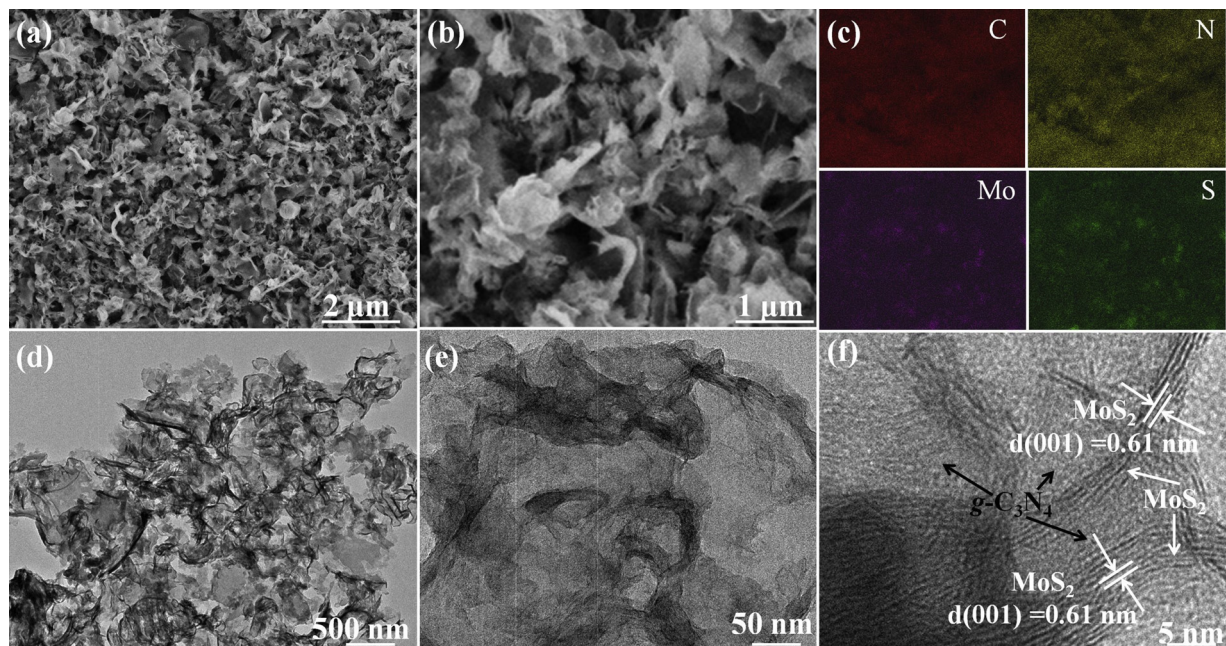


Fig. 4. (a,b) SEM images of 0.75% MoS₂/g-C₃N₄ nanosheets composite. (c) EDS elemental maps of 0.75% MoS₂/g-C₃N₄ nanosheets composite. (d,e) TEM images of 0.75% MoS₂/g-C₃N₄ nanosheets composite. (f) HRTEM image of 0.75% MoS₂/g-C₃N₄ nanosheets composite.

the highest H₂ evolution rate of 1155 $\mu\text{mol}\cdot\text{h}^{-1}$ under visible light irradiation, and the apparent yield efficiency reaches 6.8% under 420 nm monochromatic light irradiation. The H₂ evolution rate increased significantly with MoS₂ content to maximum at 0.75%, and then decreased upon further increasing MoS₂. This phenomenon could be assigned to the trade-off between the excellent H₂-generation catalytic capability and its detrimental effect on light absorption [32,33]. That is, when the amount of MoS₂ is less than 0.75%, the photocatalytic activity increases with the increased amount of MoS₂, which can be

attributed to the more exposed edge active sites for H₂ evolution reaction. However, the H₂ evolution rate decreases with the increased amount of MoS₂ when its amount is more than 0.75%, which is related to the fact that excess black MoS₂ covered on g-C₃N₄ nanosheets surface could inhibit the incident light absorption by g-C₃N₄ nanosheets. **Fig. 6c** shows the stability of photocatalytic H₂ production system using 0.75% MoS₂/g-C₃N₄ nanosheets as the photocatalyst under visible light irradiation in 0.1 M TEOA aqueous solution. As illustrated in the figure, the H₂ evolution rate during the third cycle can keep ca. 95% of the initial

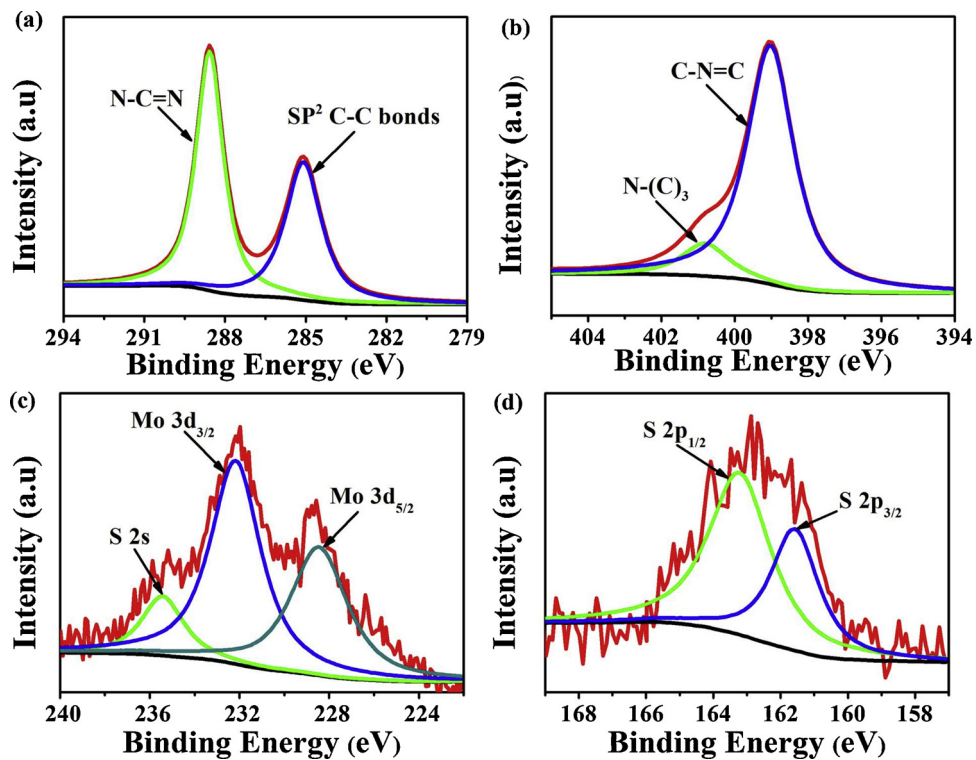
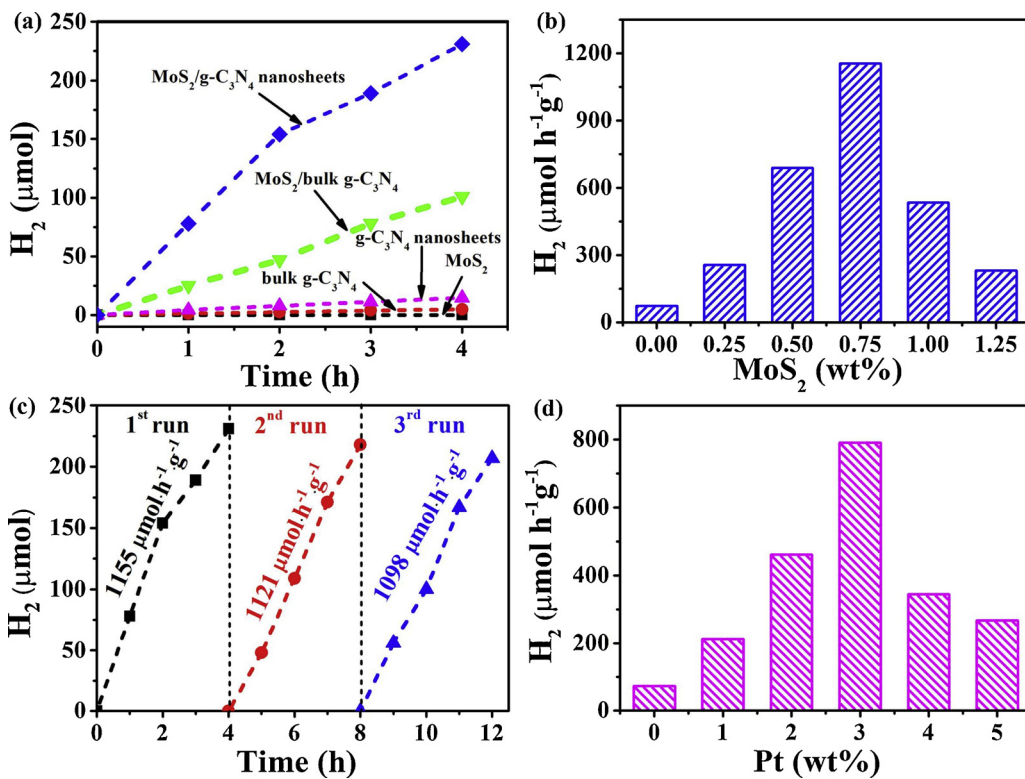


Fig. 5. HR-XPS spectrum of C 1s (a), N 1s (b), Mo 3d (c) and S 2p (d).



rate. The XRD pattern of MoS₂/g-C₃N₄ nanosheets photocatalyst after photocatalytic H₂ evolution reaction is consistent with the fresh sample, indicating the high structural stability of MoS₂/g-C₃N₄ nanosheets photocatalyst (Figure S6). The slight decrease in the H₂ generation rate could be assigned to the decreasing concentration of TEOA [34]. Furthermore, the pH may gradually change during the course of the photocatalytic H₂ evolution reaction related to the degradation of TEOA, and the pH values can effect the H⁺/H₂ reduction potential as well as TEOA⁺ deprotonation and decomposition, resulting in the slight decrease H₂ evolution rate [35].

It is known that the Pt nanoparticles is a highly-efficient cocatalyst to enhance the photocatalytic H₂ evolution activity of semiconductor photocatalysts [36,37]. For comparison, Pt nanoparticles was loaded on the surface of g-C₃N₄ nanosheets by *in situ* photodeposition method.

As shown in Fig. 6d, the maximum H₂ evolution rate of 791 μmol h⁻¹ g⁻¹ was achieved for the 3% Pt/g-C₃N₄ nanosheets photocatalyst, which is lower than the optimized MoS₂/g-C₃N₄ nanosheets photocatalyst (1155 μmol·h⁻¹ g⁻¹). To reveal the potential reasons for this phenomenon, Pt/g-C₃N₄ nanosheets was collected from the photocatalytic system after 4 h of visible light irradiation and then characterized by TEM. As illustrated in Fig. 7a,b, the aggregated Pt cocatalyst composed of nanoparticles in the size range of 3–5 nm were distributed on the surface of g-C₃N₄ nanosheets, forming a 0D-2D Pt/g-C₃N₄ nanosheets structure. The structural representation of 0D-2D Pt/g-C₃N₄ and 2D-2D MoS₂/g-C₃N₄ photocatalyst illustrated in Fig. 7c and d shows that the 0D-2D Pt/g-C₃N₄ and 2D-2D MoS₂/g-C₃N₄ photocatalyst exhibits “point contact” and “face contact” respectively. It is obviously that the 2D-2D MoS₂/g-C₃N₄ photocatalyst exhibits much more contact interfaces than that of 0D-2D Pt/g-C₃N₄ photocatalyst, and the contact interfaces act as efficient channels for charge transfer, resulting in the higher photocatalytic H₂ evolution activity of 2D-2D MoS₂/g-C₃N₄ photocatalyst. Although the photocatalytic H₂ evolution rate of as-prepared MoS₂/g-C₃N₄ photocatalyst is lower than that of Pt loaded mesoporous g-C₃N₄ nanomesh [38], it is much more higher than those previously-reported g-C₃N₄-based photocatalysts, such as MoS₂/g-C₃N₄ [5,39–41], NiS/g-C₃N₄ [42], CuS/g-C₃N₄ [43], WS₂/g-C₃N₄ [44], CoS_x/

Fig. 6. (a) Time course of H₂ evolution over different g-C₃N₄-based photocatalysts. (b) The effect of MoS₂ amount on the photocatalytic H₂ evolution performance. (c) Recycle H₂ generation property of 0.75% MoS₂/g-C₃N₄ nanosheets photocatalyst, after 4 h of irradiation and evacuation, the solution was irradiated again. (d) H₂ production rate of different Pt/g-C₃N₄ nanosheets photocatalysts.

g-C₃N₄ (Table S1) [45].

The positive slope of Mott-Schottky plot at frequency of 2.0 kHz in Fig. 8a reveals n-type semiconductor characteristics for g-C₃N₄ nanosheets. The conduction band and valance band potential of g-C₃N₄ nanosheets is calculated to be -1.42 V and 1.44 V (vs. Ag/AgCl, pH 6.6), respectively. The reaction mechanism for photocatalytic H₂ production over MoS₂/g-C₃N₄ nanosheets photocatalysts was illustrated in Fig. 8b. The g-C₃N₄ acting as a light-harvesting semiconductor absorbs irradiated light to generate electron-hole pairs. The photoelectrons can be transferred from g-C₃N₄ to MoS₂ because the g-C₃N₄ has a more negative conduction band level than that of MoS₂ [E_{CB}(MoS₂) = -0.67 V vs. Ag/AgCl, pH 6.6, Figure S7]. Furthermore, the 2D nanointerfaces exhibited in MoS₂/g-C₃N₄ nanosheets photocatalysts provide abundant channel for charge transfer, improving the separation efficiency of photogenerated electron-hole pairs. Owing to the more negative reduced potential of H⁺/H₂ [E(H⁺/H₂) = -0.59 V vs. Ag/AgCl, pH 6.6] [46]. The MoS₂ serving as a highly-efficient H₂-generation reaction catalyst which reduces protons to evolve H₂ after it accepts electrons from g-C₃N₄. Because the valance band level of g-C₃N₄ [E_{VB}(g-C₃N₄) = +1.44 V vs. Ag/AgCl, pH 6.6] is more positive than the oxidation potential of TEOA [E(TEOA⁺/TEOA) = +0.82 V vs. NHE, pH 0, +0.34 V vs. Ag/AgCl, pH 6.6] [47], the holes in the valance band of g-C₃N₄ can oxidize the TEOA to regenerate the ground-state g-C₃N₄. photoluminescence (PL) and time-decay fluorescence spectra are used to confirm the efficient electron transfer from g-C₃N₄ to MoS₂. As shown in Fig. 8c, the emission intensity of MoS₂/g-C₃N₄ nanosheets photocatalysts decreases with the increasing amount of MoS₂. Because the fluorescence emission results from the recombination of free electron and hole, the quenching of photoluminescence suggests that the photogenerated electrons of g-C₃N₄ nanosheets can be efficiently transferred to MoS₂ [48,49]. To better understand the photoexcited charge carriers transfer process, the time-resolved emission decay spectra of all MoS₂/g-C₃N₄ nanosheets photocatalysts were recorded, and the results were shown in Fig. 8d. The lifetimes were obtained by fitting the time-decay fluorescence curves using a single-exponential function. The PL lifetimes of bare g-C₃N₄, 0.25%, 0.50%, 0.75%, 1.00% and 1.25%

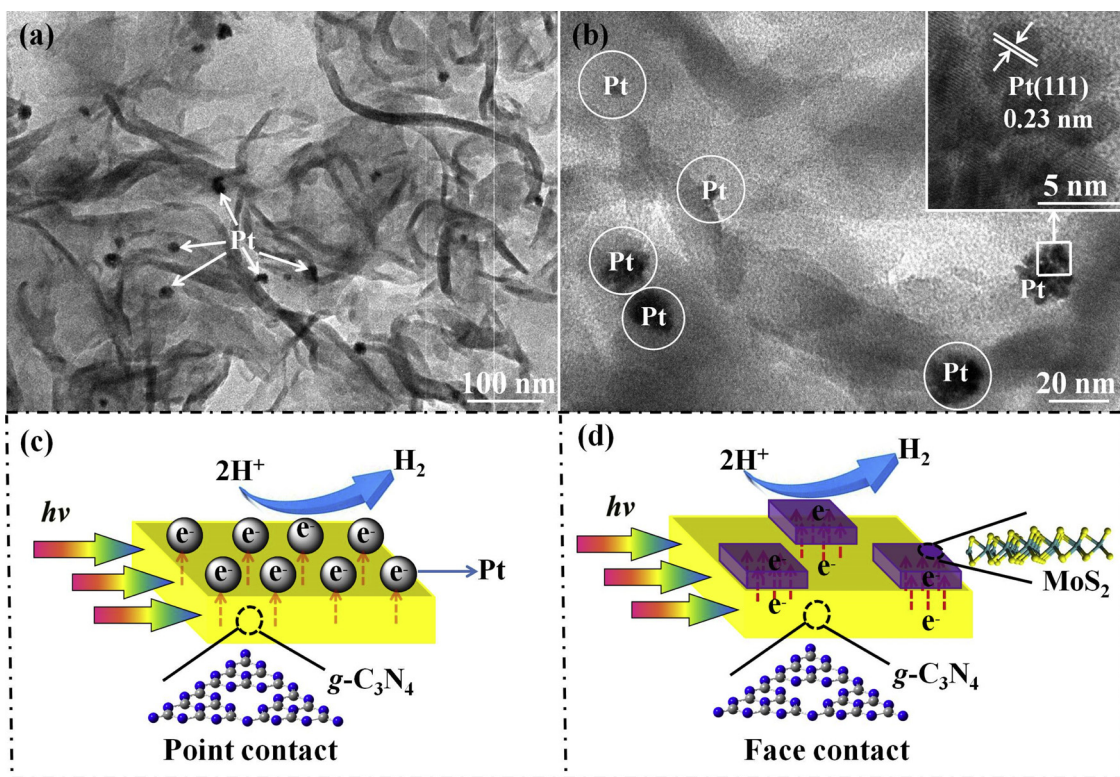


Fig. 7. (a,b) TEM images of 3% Pt/g-C₃N₄ nanosheets photocatalyst. Inset in Fig. 7b shows the Pt nanoparticles with a lattice spacing of 0.23 nm. (c and d) Schematic diagrams of 0D-2D Pt/g-C₃N₄ nanosheets photocatalysts and 2D-2D MoS₂/g-C₃N₄ nanosheets photocatalysts, which clearly shows that the 2D-2D MoS₂/g-C₃N₄ photocatalyst exhibits much larger contact surface for interfacial charge transfer in comparison to those 0D-2D Pt/g-C₃N₄ nanosheets photocatalysts.

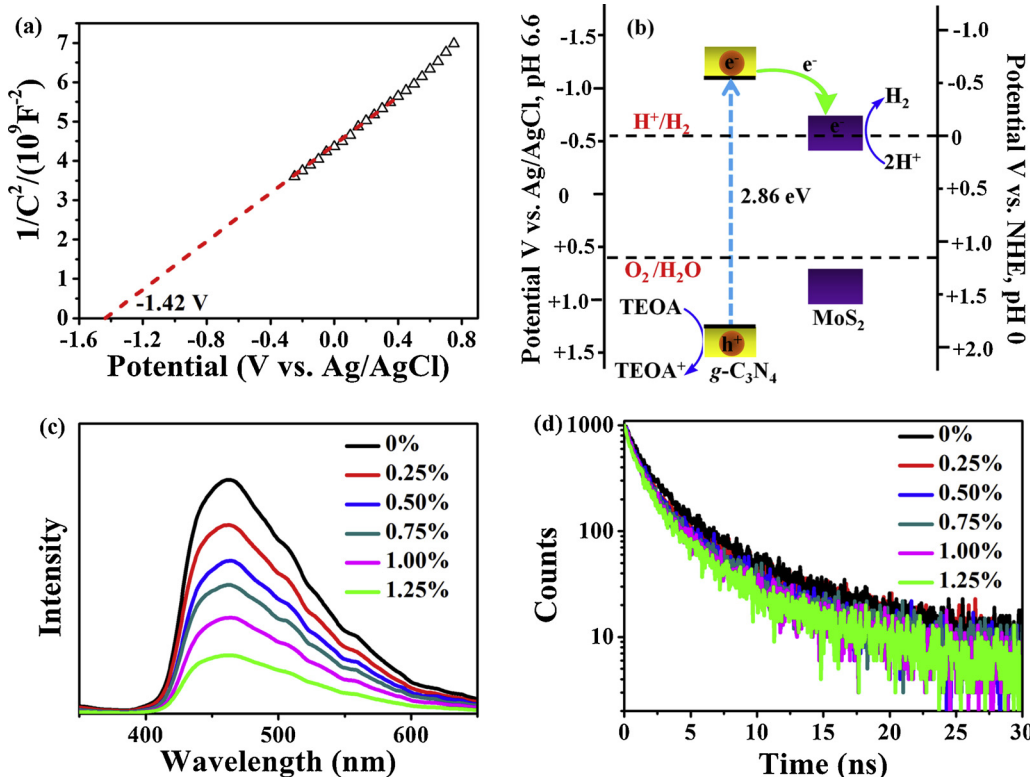


Fig. 8. (a) Mott-Schottky plots of g-C₃N₄ nanosheets in 0.5 M Na₂SO₄ aqueous solution. (b) Schematic energy-level diagrams of MoS₂ and g-C₃N₄ in comparison with the H⁺/H₂ and O₂/H₂O redox potentials. (c) Fluorescence emission spectra of MoS₂/g-C₃N₄ nanosheets loading with various amounts of MoS₂. (d) Time-resolved fluorescence spectra of different MoS₂/g-C₃N₄ nanosheets photocatalysts loading with various amounts of MoS₂.

MoS₂/g-C₃N₄ were calculated to be 2.35, 2.22, 2.11, 2.02, 1.88 and 1.79 ns, respectively. The PL lifetimes decreased with the increasing amount of MoS₂, indicating that the positive role of MoS₂ in improving the separation efficiency of free charge carriers.

4. Conclusion

In conclusion, g-C₃N₄ nanosheets with high surface area were prepared by a simple probe sonication assisted liquid exfoliation method,

and the photocatalytic activity for H₂ production of surface-dependent g-C₃N₄ coupled with MoS₂ cocatalyst were systematically studied. The MoS₂/g-C₃N₄ nanosheets showed the highest photocatalytic performance with a H₂ generation rate of 1155 μmol·h⁻¹ g⁻¹, which is much higher than that of the optimized Pt-loaded g-C₃N₄ nanosheets photocatalyst. The apparent quantum yield at 420 nm reaches 6.8%. The excellent photocatalytic performance of MoS₂/g-C₃N₄ nanosheets is related to the large surface area of g-C₃N₄ nanosheets as well as the large 2D nanointerface between MoS₂ and g-C₃N₄ nanosheets. This work shows that this kind of 2D-2D MoS₂/g-C₃N₄ nanosheets photocatalysts have great potential for the solar H₂ generation.

Conflict of interest

The authors declare no competing financial interest.

Acknowledgments

This research was supported by the National Natural Science Foundation of China under Grant No. 51772071, 51502068 and 51802063, the Natural Science Foundation of Zhejiang Province under Grant No. LQ19E020002 and LQ19E020007 and the Research Foundation from the State Key Lab of Silicon Materials (SKL2018-01).

Appendix A. Supplementary data

Supplementary material related to this article can be found, in the online version, at doi:<https://doi.org/10.1016/j.apcatb.2019.01.043>.

References

- Y. Ma, X.L. Wang, Y.S. Jia, X.B. Chen, H.X. Han, C. Li, Titanium dioxide-based nanomaterials for photocatalytic fuel generations, *Chem. Rev.* 114 (2014) 9987–10043.
- Y.J. Yuan, Z.T. Yu, D.Q. Chen, Z.G. Zou, Metal-complex chromophores for solar hydrogen generation, *Chem. Soc. Rev.* 46 (2017) 603–631.
- M. Xiao, Z. Wang, M. Lyu, B. Luo, S. Wang, G. Liu, H.M. Cheng, L. Wang, Hollow nanostructures for photocatalysis: advantages and challenges, *Adv. Mater.* 31 (2019) 1801369.
- X. Wang, K. Maeda, A. Thomas, K. Takanabe, G. Xin, J.M. Carlsson, K. Domen, M. Antonietti, A metal-free polymeric photocatalyst for hydrogen production from water under visible light, *Nat. Mater.* 8 (2009) 76–82.
- X. Shi, M. Fujitsuka, S. Kim, T. Majima, Faster Electron injection and more active sites for efficient photocatalytic H₂ evolution in g-C₃N₄/MoS₂ hybrid, *Small* 14 (2018) 1703277.
- P.F. Xia, M.J. Liu, B. Cheng, J.G. Yu, L.Y. Zhang, Template-free synthesis of hollow G-C₃N₄ polymer with vesicle structure for enhanced photocatalytic water splitting, *J. Phys. Chem. C* 122 (2018) 3786–3793.
- L.H. Lin, W. Ren, C. Wang, A.M. Asiri, J. Zhang, X.C. Wang, Crystalline carbon nitride semiconductors prepared at different temperatures for photocatalytic hydrogen production, *Appl. Catal. B: Environ.* 231 (2018) 234–241.
- H. Ou, L. Lin, Y. Zheng, P. Yang, Y. Fang, X. Wang, Tri-s-triazine-Based crystalline carbon nitride nanosheets for an improved hydrogen evolution, *Adv. Mater.* 29 (2017) 1700008.
- Q. Liang, Z. Li, Z.H. Huang, F. Kang, Q.H. Yang, Holey graphitic carbon nitride nanosheets with carbon vacancies for highly improved photocatalytic hydrogen production, *Adv. Funct. Mater.* 25 (2015) 6885–6892.
- Y.J. Yuan, Y. Yang, Z.J. Li, D.Q. Chen, S.T. Wu, G.L. Fang, W.F. Bai, M.Y. Ding, L.X. Yang, D.P. Cao, Z.T. Yu, Z.G. Zou, Promoting charge separation in g-C₃N₄/Graphene/MoS₂ photocatalysts by two-dimensional nanojunction for enhanced photocatalytic H₂ production, *ACS Appl. Energy Mater.* 1 (2018) 1400–1407.
- J.H. Zhang, Y.J. Hou, S.J. Wang, X.J. Zhu, C.Y. Zhu, Z. Wang, C.J. Li, J.J. Jiang, H.P. Wang, M. Pan, C.Y. Su, A facile method for scalable synthesis of ultrathin g-C₃N₄ nanosheets for efficient hydrogen production, *J. Mater. Chem. A Mater. Energy Sustain.* 6 (2018) 18252–18257.
- T.F. Ma, J. Bai, Q. Wang, C.P. Li, The novel synthesis of a continuous tube with laminated g-C₃N₄ nanosheets for enhancing photocatalytic activity and oxygen evolution reaction performance, *Dalton Trans.* 47 (2018) 10240–10248.
- H. Huang, K. Xiao, N. Tian, F. Dong, T. Zhang, X. Du, Y. Zhang, Template-free precursor-surface-Etching route to porous, thin g-C₃N₄ nanosheets for enhancing photocatalytic reduction and oxidation activity, *J. Mater. Chem. A Mater. Energy Sustain.* 5 (2017) 17452–17463.
- J. Xu, L.W. Zhang, R. Shi, Y.F. Zhu, Chemical exfoliation of graphitic carbon nitride for efficient heterogeneous photocatalysis, *J. Mater. Chem. A Mater. Energy Sustain.* 1 (2013) 14766–14772.
- F. Cheng, H. Wang, X. Dong, The amphoteric properties of g-C₃N₄ nanosheets and fabrication of their relevant heterostructure photocatalysts by an electrostatic Re-assembly route, *Chem. Commun.* 51 (2015) 7176–7179.
- P. Niu, L. Zhang, G. Liu, H.M. Cheng, Graphene-like carbon nitride nanosheets for improved photocatalytic activities, *Adv. Funct. Mater.* 22 (2012) 4763–4770.
- S. Yang, Y. Gong, J. Zhang, L. Zhan, L. Ma, Z. Fang, R. Vajtai, X. Wang, P.M. Ajayan, Exfoliated graphitic carbon nitride nanosheets as efficient catalysts for hydrogen evolution under visible light, *Adv. Mater.* 25 (2013) 2452–2456.
- S. Zhang, X. Liu, C. Liu, S. Luo, L. Wang, T. Cai, Y. Zeng, J. Yuan, W. Dong, Y. Pei, Liu, Y. MoS₂ quantum dot growth induced by S vacancies in a ZnIn₂S₄ monolayer: atomic-level heterostructure for photocatalytic hydrogen production, *ACS Nano* 12 (2018) 751–758.
- Y.J. Yuan, Z.J. Ye, H.W. Lu, B. Hu, Y.H. Li, D.Q. Chen, J.S. Zhong, Z.T. Yu, Z.G. Zou, Constructing anatase TiO₂ nanosheets with exposed (001) facets/Layered MoS₂ two-dimensional nanojunctions for enhanced solar hydrogen generation, *ACS Catal.* 6 (2016) 532–541.
- Y.J. Yuan, P. Wang, Z.J. Li, Y.Z. Wu, W.F. Bai, Y.B. Su, J. Guan, S.T. Wu, J.S. Zhong, Z.T. Yu, Z.G. Zou, The role of Bandgap and interface in enhancing photocatalytic H₂ generation activity of 2D-2D black Phosphorus/MoS₂ photocatalyst, *Appl. Catal. B: Environ.* 242 (2019) 1–8.
- J.W. Shi, Y. Zou, D. Ma, Z. Fan, L. Cheng, D. Sun, Z. Wang, C. Niu, L. Wang, Stable 1T-phase MoS₂ as an effective Electron mediator promoting photocatalytic hydrogen production, *Nanoscale* 10 (2018) 9292–9303.
- J. Liu, Y. Liu, N. Liu, Y. Han, X. Zhang, H. Huang, Y. Lifshitz, S.T. Lee, J. Zhong, Z.H. Kang, Metal-free efficient photocatalyst for stable visible water splitting via a two-electron pathway, *Science* 27 (2015) 970–974.
- Y. Cao, Z. Zhang, J. Long, J. Liang, H. Lin, H. Lin, X. Wang, Vacuum heat-treatment of carbon nitride for enhancing photocatalytic hydrogen evolution, *J. Mater. Chem. A Mater. Energy Sustain.* 2 (2014) 17797–17807.
- S. Yang, Y. Gong, J. Zhang, L. Zhan, L. Ma, Z.Y. Fang, Vajtai R, Exfoliated graphitic carbon nitride nanosheets as efficient catalysts for hydrogen evolution under visible light, *Adv. Mater.* 25 (2013) 2452–2456.
- J. Mao, T.Y. Peng, X.H. Zhang, K. Li, L.Q. Ye, L. Zan, Effect of graphitic carbon nitride microstructures on the activity and selectivity of photocatalytic CO₂ reduction under visible light, *Catal. Sci. Technol.* 3 (2013) 1253–1260.
- X. Fan, P. Xu, Y. Zhou, Y.C. Sun, M.A.T. Li, M. Nguyen, T.E. Terrones, Mallouk, fast and efficient preparation of exfoliated 2H MoS₂ nanosheets by sonication-assisted lithium intercalation and infrared laser-induced 1T to 2H phase reversion, *Nano Lett.* 15 (2015) 5956–5960.
- Y.J. Yuan, D.Q. Chen, Y. Huang, Z.T. Yu, J.S. Zhong, T.T. Chen, W.G. Tu, Z.J. Guan, D.P. Cao, Role of two-dimensional nanointerfaces in enhancing the photocatalytic performance of 2D-2D MoS₂/CdS photocatalysts for H₂ production, *Chem. Eng. J.* 350 (2018) 335–343.
- X. Lu, Y. Jin, X. Zhang, Gg Xu, D. Wang, J. Lv, Z. Zheng, Y. Wu, Controllable synthesis of graphitic C₃N₄/Ultrathin MoS₂ nanosheet hybrid nanostructures with enhanced photocatalytic performance, *Dalton Trans.* 45 (2016) 15406–15414.
- Y. Zou, J. Shi, D. Ma, Z. Fan, C. He, L. Cheng, D. Sun, J. Li, Z. Wang, C. Niu, Efficient spatial charge separation and transfer in ultrathin g-C₃N₄ nanosheets modified with Cu₂MoS₄ as a noble metal-free Co-catalyst for superior visible light-driven photocatalytic water splitting, *Catal. Sci. Technol.* 8 (2018) 3883–3893.
- L. He, B. Cui, J. Liu, M. Wang, Z. Zhang, H. Zhang, Fabrication of porous CoO_x/mC₆₀/MoS₂ composite loaded on g-C₃N₄ nanosheets as a highly efficient dual electrocatalyst for oxygen reduction and hydrogen evolution reactions, *ACS Sustain. Chem. Eng.* 6 (2018) 9257–9268.
- M. Wang, P. Ju, J. Li, Y. Zhao, X. Han, Z. Hao, Facile synthesis of MoS₂/g-C₃N₄/GO ternary heterojunction with enhanced photocatalytic activity for water splitting, *ACS Sustain. Chem. Eng.* 5 (2017) 7878–7886.
- N.T. Nguyen, M. Altomare, J. Yoo, P. Schmuki, Efficient photocatalytic H₂ evolution: controlled dewetting-dealloying to fabricate site-selective high-activity nanoporous Au particles on highly ordered TiO₂ nanotube arrays, *Adv. Mater.* 27 (2015) 3208–3215.
- Y. Zou, J.W. Shi, D. Ma, Z. Fan, C. Niu, L. Wang, Fabrication of g-C₃N₄/Au/C-TiO₂ hollow structures as visible-light-Driven Z-Scheme photocatalysts with enhanced photocatalytic H₂ evolution, *ChemCatChem* 9 (2017) 3752–3761.
- T. Zhou, Y. Du, A. Borgna, J. Hong, Y. Wang, J. Han, W. Zhang, R. Xu, Post-synthesis modification of a metal-organic framework to construct a bifunctional photocatalyst for hydrogen production, *Energy Environ. Sci.* 6 (2013) 3229–3234.
- D. Lu, H. Wang, X. Zhao, K.K. Kondamareddy, J. Ding, C. Li, P. Fang, Highly efficient visible-light-Induced photoactivity of Z-Scheme g-C₃N₄/Ag/MoS₂ ternary photocatalysts for organic pollutant degradation and production of hydrogen, *ACS Sustain. Chem. Eng.* 5 (2017) 1436–1445.
- T. Simon, M.T. Carlson, J.K. Stolarczyk, J. Feldmann, Electron transfer rate vs recombination losses in photocatalytic H₂ generation on Pt-Decorated CdS nanorods, *ACS Energy Lett.* 1 (2016) 1137–1142.
- Y. Cao, D. Wang, Y. Lin, W. Liu, L. Cao, X. Liu, W. Zhang, X. Mou, S. Fang, X. Shen, T. Yao, Single Pt atom with highly vacant d-Orbital for accelerating photocatalytic H₂ evolution, *ACS Appl. Energy Mater.* 1 (2018) 6082–6088.
- Q. Han, B. Wang, J. Gao, Z. Cheng, Y. Zhao, Z. Zhang, L. Qu, Atomically thin mesoporous nanomesh of graphitic C₃N₄ for high-efficiency photocatalytic hydrogen evolution, *ACS Nano* 10 (2016) 2745–2751.
- L. Ge, C. Han, X. Xiao, L. Guo, Synthesis and characterization of composite visible light active photocatalysts MoS₂-g-C₃N₄ with enhanced hydrogen evolution activity, *Int. J. Hydrogen Energy* 38 (2013) 6960–6969.
- N. Li, J. Zhou, Sheng Z, W. Xiao, Molten salt-mediated formation of g-C₃N₄-MoS₂ for visible-light-Driven photocatalytic hydrogen evolution, *Appl. Surf. Sci.* 430 (2018) 218–224.
- Y.D. Hou, A.B. Laursen, J.S. Zhang, G.G. Zhang, Y.S. Zhu, X.C. Wang, S. Dahl,

I. Chorkendorff, Layered nanojunctions for hydrogen-evolution catalysis, *Angew. Chem. Int. Ed.* 52 (2013) 3621–3625.

[42] Z. Chen, P. Sun, B. Fan, Z. Zhang, X. Fang, In situ template-free ion-exchange process to prepare visible-light-Active g-C₃N₄/NiS hybrid photocatalysts with enhanced hydrogen evolution activity, *J. Phys. Chem. C* 118 (2014) 7801–7807.

[43] R. Shen, J. Xie, P. Guo, L. Chen, X. Chen, X. Li, Bridging the g-C₃N₄ nanosheets and robust CuS cocatalysts by metallic acetylene black interface mediators for active and durable photocatalytic H₂ production, *ACS Appl. Energy Mater.* 1 (2018) 2232–2241.

[44] M.S. Akple, J. Low, S. Wageh, A.A. Al-Ghamdi, J. Yu, J. Zhang, J. Enhanced Visible Light Photocatalytic H₂ Production of g-C₃N₄/WS₂ Composite Heterostructures, *Appl. Surf. Sci.* 358 (2015) 196–203.

[45] J. Fu, C. Bie, B. Cheng, C. Jiang, J. Yu, Hollow CoS_x polyhedrons act as high-efficiency cocatalyst for enhancing the photocatalytic hydrogen generation of g-C₃N₄.

ACS Sustain. Chem. Eng. 6 (2018) 2767–2779.

[46] J.S. Zhang, X.F. Chen, K. Takanabe, K. Maeda, K. Domen, J.D. Epping, X.Z. Fu, M. Antonietti, X.C. Wang, Synthesis of a carbon nitride structure for visible-light catalysis by copolymerization, *Angew. Chem. Int. Ed.* 49 (2010) 441–444.

[47] Y.J. Yuan, Z.T. Yu, J.G. Cai, C. Zheng, W. Huang, Z.G. Zou, Water reduction systems associated with homoleptic cyclometalated iridium complexes of various 2-Phenylpyridines, *ChemSusChem* 6 (2013) 1357–1365.

[48] L. Ge, C. Han, X. Xiao, L. Guo, In situ synthesis of cobalt-phosphate (Co-Pi) modified g-C₃N₄ photocatalysts with enhanced photocatalytic activities, *Appl. Catal. B: Environ.* 142–143 (2013) 414–422.

[49] C. Li, Y. Du, D. Wang, S. Yin, W. Tu, Z. Chen, M. Kraft, G. Chen, R. Xu, Unique P-Co-N surface bonding states constructed on g-C₃N₄ nanosheets for drastically enhanced photocatalytic activity of H₂ evolution, *Adv. Funct. Mater.* 13 (2017) 1604328.